Kinematics and Statistics of Breaking Waves Observed Using SWIFT Buoys

Adam Brown ⓘ, Jim Thomson, Ashley Ellenson, Fadia Ticona Rollano, H. Tuba Özkan-Haller, and Merrick C. Haller

Abstract—Surface wave instrumentation floats with tracking were deployed by helicopter ahead of five large storms off the Oregon coast. The buoys drifted freely with the wave motions, surface currents, and wind. The buoys use a 9-DoF inertial measurement unit that fuses the measurements of accelerometers, magnetometers, and gyroscopes to measure acceleration in the global North-West-Up reference frame. Rapid sampling (25 Hz) allows for the observation of both propagating wave motions and wave breaking events. Bulk wave parameters and wave spectra are calculated from the motion of the buoys using conventional methods, and breaking wave impacts are identified in the raw acceleration data using a new algorithm based on a short-time Fourier transform. The number of breaking waves is used to infer breaker fraction, which is found to depend on bulk wave steepness as previously shown in the literature. The magnitude and duration of acceleration during breaking is used in a new quantification of breaker intensity, which increases with wave height, period, and steepness. There is significant variance of breaker intensity in a given wave field, such that intense breakers still occur in relatively mild wave fields. The buoy observations are compared to the output of the WaveWatch III forecast model, with evaluation of an empirical breaker prediction scheme applied to WaveWatch III output.

Index Terms—Buoy, breaking, breaker, identification, intensity, measurement, ocean, probability, severity, wave.

I. INTRODUCTION

BREAKING waves pose a significant threat to ships and platforms in the ocean. An intense impact load is generated during a breaking wave strike that acts above the water line. The impact may directly cause damage, or the load accompanied by the steep surface of the wave crest can lead to capsizing [1]–[4]. Designing an offshore system to withstand breaking waves requires a quantification of the frequency and intensity of breaking waves [5]. Breaking waves are also the primary mechanism of energy dissipation and momentum transfer from waves to the upper ocean [6]–[10].

One particular application for wave breaking prediction is related to the conversion of wave energy for electricity. Systems designed to harvest energy from ocean waves are called wave energy converters (WECs). To date, most WECs have been deployed at designated wave energy test sites. These sites support the WEC developers by providing local knowledge and outreach, deployment and recovery infrastructure, and a grid connection. The U.S. Department of Energy has funded the development of a grid connected wave energy test site about 10-km offshore of Newport, OR, USA, that will be operated by Oregon State University. The site formerly known as the Pacific Marine Energy Center's South Energy Test Site, has recently been renamed PacWave. The site, shown in Fig. 1, has water depths ranging across a gentle slope from 40 m on the seaward side to 30 m on the shoreward side. Similar to many of the locations proposed for commercial wave energy development, the Oregon coast is highly energetic and the wave resource has a strong seasonal dependence [11]. The average significant wave height (H_s) at the site is approximately 2 m during the summer and 4 m during the winter. Each year, several strong winter storms generate wave heights in excess of 8 m. These storms often have wind speeds of 25 m/s or more, and generate waves that transport an order of magnitude more energy than those during calm conditions. Breaking waves during these storms vary greatly in size and intensity; ranging from barely visible whitecaps on steep wave crests, to towering plunging breakers that generate persistent bubble plumes (see Fig. 2).

Surface wave instrumentation floats with tracking (SWIFTs) were deployed by helicopter ahead of five large storms impacting PacWave in the winters of 2015, 2016, and 2017 (see Fig. 1). SWIFTs have been used around the world for various studies focused on wave measurement, breaking waves, and the propagation of waves through partial ice cover [6], [12], [13]. The SWIFTs include an inertial measurement unit (IMU) that fuses the measurements of accelerometers, gyroscopes, and magnetometers to estimate the orientation of the buoy in the global North-West-Up (NWU) reference frame. SWIFTs are fully capable of directional wave measurements, using the methods of Herbers *et al.* [14], that have been shown to produce results within 5% of Datawell Waverider measurements. A direct comparison of SWIFT and Waverider measurements was performed by Thomson *et al.* [15, Fig. 1] and by Schwendeman and Thomson [16, Figs. 3 and 5].

In addition to providing standard wave measurements, the SWIFT accelerations can be used to identify impulsive breaking wave impacts. The transient acceleration signal of a breaking wave is distinct from that of the propagating waves appearing at much higher frequencies. Cameras mounted to a short mast recorded images of the water surface every 4–6 s through-
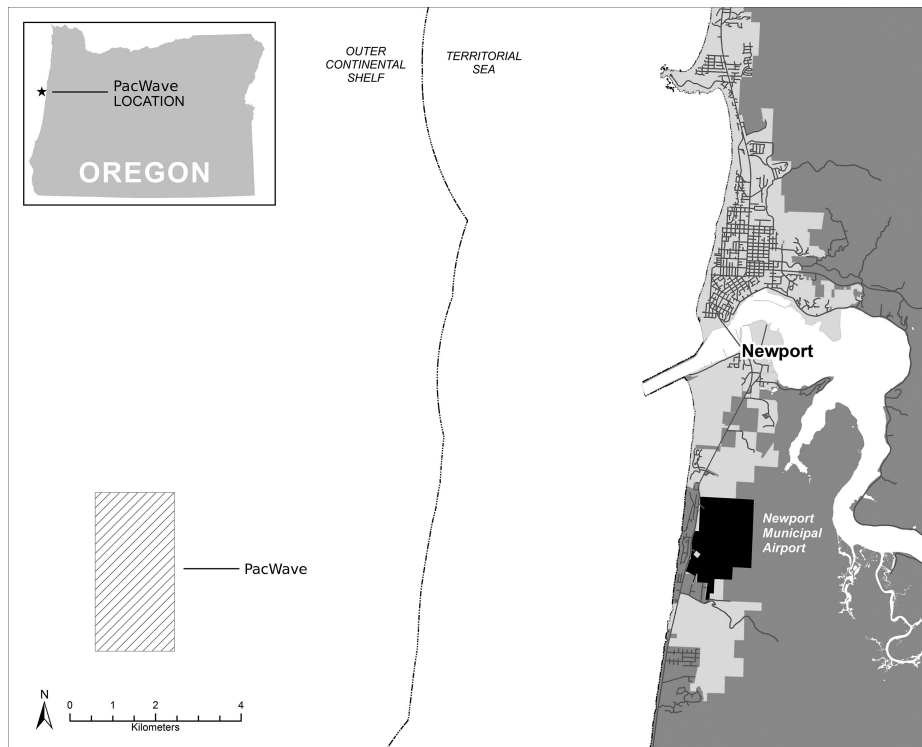
Fig. 1.   Location of PacWave is shown relative to the town of Newport, OR, USA.

Fig. 2.   Top: A SWIFT is impacted by a small breaking crest as a larger breaking wave approaches. Bottom: A SWIFT on the beach after drifting back to shore.

out the deployment. During daylight, the images are used to corroborate breaking wave events identified in the acceleration data.

In Section II, we provide a literature review of buoy-based breaking wave detection methods and experimental observations of breaker probability. Section III provides a discussion of the wave measurements made at PacWave and the method used to detect breaking waves in SWIFT acceleration data. The results are presented in Section IV where both the occurrence and strength of breaking events are empirically related to the measured bulk parameters of the wave field. Finally, the results are extended to modeled bulk parameters of the wave field, as demonstration of a possible future application.

II. LITERATURE REVIEW

A. Buoy-Based Breaker Detection Methods

Wave measurement buoys are deployed around the world providing measurements of the sea surface, even in conditions where other systems fail. Commercial buoys typically sample at rates between 1 and 4 Hz; providing bulk and spectral measurements of the wave field. However, buoys that are capable of sampling at higher rates can also be used to identify breakers and to quantify their kinematics. Longuet-Higgins and Smith used a capacitive wire gauge mounted to a spar buoy to detect breaking waves in the field [17]. Breakers were identified based on rapid jumps in the measured sea surface elevation. The results of the experiment seem roughly in line with the breaking rates found by other studies, although a thorough accounting of the wind and wave conditions during each deployment is not provided. A fundamental challenge to the effective use of wire gauge systems relates to controlling the motion of the buoy. To accurately measure wave height and jumps in surface

elevation, the spar must remain vertical in extreme waves. Furthermore, buoy motion will to some extent always be excited by the waves. Therefore, the heave of the buoy itself can affect the measurements of wave height and surface jumps.

Gemmrich and Farmer used a conductivity sensor mounted to a freely drifting buoy to detect rapid changes in the void fraction of the water surface due to breaking waves [18]. The study demonstrated that breaking frequency is highly correlated to the energy input to the waves from the wind. Void fraction systems may falsely identify some waves as breaking if the buoys drift into persistent bubble plumes. This method may also miss some waves that impact the buoy at the inception of breaking before the development of a turbulent crest. For this reason void fraction sensors are most effectively used in combination with other sensor technologies.

To bypass the complications of a moving test platform, Weissman *et al.* mounted a wire gauge to the side of a stationary platform to measure breaking waves in Lake Washington [19]. Measurements were made at high frequency, and breakers were identified based on energy content in the frequency band from 18 to 32 Hz. The experimental results from this study are limited, and due to the test location and conditions, the measured breaking waves were small. It was found that in the given wind driven seas 1.2% of the measured wave crests were breaking. This is a relatively high fraction of breaking waves compared to more recent studies, possibly due to the relatively high rate of wind energy input to small waves at the fetch limited test location.

Pascal *et al.* built a spar buoy that incorporated both an IMU and a wire gauge [20]. The measurements of the wire gauge sensor were corrected based on the acceleration and orientation of the spar measured by the IMU. A wave surface slope threshold was used to identify breaking waves in the motion corrected wire gauge data.

Balaji *et al.* tested a scaled buoy subject to steep, spilling, and plunging breakers in a wave flume [21]. The buoy was attached to potentiometers using a system of cables and pulleys. The potentiometers were used to record the motion of the buoy, and wavelet and spectral analysis were used to analyze the motion of the buoy induced by breaking waves. Changes in the phasing of high-frequency wave components were detected and used to identify breakers.

Thomson has deployed SWIFT drifters for various studies around the globe [12]. These small spar type buoys can house multiple sensor payloads depending on the study [6], [13]. SWIFTs were primarily developed to measure the turbulence generated by breaking waves, using an AquadoppHR mounted 1 m below the water surface looking either up or down. SWIFTs also house a 9-DoF IMU that records the acceleration and orientation of the hull at frequencies up to 200 Hz. The turbulence generated by breaking waves and measured by the SWIFTs can be used to calculate a partial estimate of the energy dissipated by the wave.

The studies discussed above focused on breaking waves in deep-water. However, it may be more practical to develop and test technologies for breaker detection in the surf zone where wave breaking is frequent and predictable, allowing a device to measure many breaking waves in a short period of time.

Although the mechanisms of energy transfer to the wave crest vary with water depth, the final release and dissipation of energy by a breaking crest are similar regardless of depth.

With the help of a few surfers, Sinclair deployed an 8.75-cm diameter Lagrangian float called the FlowRider in the surf zone at Waimea Bay, HI, USA [22]. Although a 9-DoF IMU was integrated into the float, the acceleration signals recorded in the sensor reference frame were not converted to the global reference frame. Still, plunging breakers were successfully identified based on a drop to zero g accelerations as the drifter was swept over the barrel of the wave, and high-amplitude, high-frequency accelerations as the FlowRider impacted the water in front of the breaker.

Brown deployed a custom spherical wave measurement buoy in the surf zone off Agate Beach near Newport, OR, USA [23]. The buoy was approximately 50 cm in diameter and was deployed both moored and free-drifting. The buoy housed a 9-DoF IMU sampling at frequencies of 100 Hz or more. Recorded accelerations were converted to the global NWU reference frame. The impacts of more than 300 breaking waves were recorded, and the signatures of incipient, spilling, and plunging breakers were characterized in the data. The mooring was found to have little effect on the breaking signature. The research was conducted as a first step in the development of a buoy capable of determining site specific breaker probabilities during multiyear deployments in remote locations.

The buoy studies mentioned above used sampling frequencies much higher than commercial wave measurement buoys. For reference, directional Datawell Waverider buoys commonly operate at an output frequency of 1.28 Hz [24]. The Triaxys directional wave sensor has a default sampling frequency of 4 Hz, but can be deployed with a maximum sampling frequency up to 10 Hz [25]. As the impact of breaking waves is of short duration and excites high-frequency motion above the natural frequency of the buoys, high-frequency sampling is critical to the detection of breaking waves in acquired data.

B. Breaker Probability and Bulk Parameterizations

Both Zippel and Thomson and Schwendeman and Thomson provide reviews of the literature focused on breaker probability and dissipation [6], [26]. Here, we will focus on a few relevant parameterizations and findings that relate wave breaking to common statistical measures of ocean waves.

Breaker rate is defined as the number of breakers observed during an observation period, divided by the duration of the observation [27]. The value is usually reported with units of per hour. However, breaking wave studies have been conducted in a multitude of locations and conditions. If more waves at a higher frequency pass a given location, more breaking waves will be observed. To more directly compare studies, breaker rate can be normalized by the average or peak period of the waves. The resulting breaker probability is usually reported as the fraction of waves passing a spot on the water surface that are breaking, and is called the breaker fraction (Q_b)

$$Q_b = N_b T / \tau \qquad (1)$$

where N_b is the number of observed breakers, T is the period of the waves, and τ is the period of observation. In random seas, various average wave periods can be derived from the omnidirectional wave spectrum. The wave period most commonly applied to the derivation of breaker fraction is the peak period (T_p), which is defined as the inverse of the most energetic spectral frequency. However, as wave spectra are discretized in frequency, T_p will also be discretized. To avoid discretization error, an approximation of T_p, derived from the moments of the omnidirectional energy spectrum ($E(f)$), will be used throughout this paper [28, Sec. 2.3.2]

$$T_p \approx m_{-2} m_1 / m_0^2 \qquad (2)$$

where

$$m_N = \int_{f_{\min}}^{f_{\max}} f^N E(f)\, df \qquad (3)$$

is the Nth spectral moment for a spectrum spanning a range of frequencies from $f_{\min}$ to $f_{\max}$.

Previous studies have shown that Q_b is highly correlated with bulk measures of the steepness of the wave field [29]. One measure of wave field steepness, based on the Miche limiting steepness, is

$$\bar{S} = H_s k_m / \tan h(k_m d) \qquad (4)$$

where k_m is the wave number associated with a wave of average period ($T_m = m_0 / m_1$). $\bar{S}$ has been used by Chawla and Kirby and Zippel and Thomson [6], [30].

In deep-water, the majority of breaking in random seas occurs in the higher frequency components of the wave field and is centered at frequencies greater than two times the peak wave frequency [31]. Thus, k_m is closer to the wave number of the average breaking wave than k_p, and will be used for the calculation of steepness in this paper.

The mean-square slope (MSS) is another measure of wave field steepness [27]. It is closely related to the spectral saturation parameter (σ) used by Banner and Morison [31]

$$\sigma(f) = (2\pi)^4 f^5 E(f) / (2g^2) \qquad (5)$$

where

$$\text{MSS} = \int_{f_{\min}}^{f_{\max}} \frac{2\sigma(f)}{f}\, df = (2\pi)^4 M_4 / g^2. \qquad (6)$$

For this work, MSS is calculated over the full bandwidth of the spectrum ($0.0333 < f < 0.5$), although some other studies use only $f > f_p$.

Experimentally, MSS has been shown to depend on wind speed (U_{10}) through a log relation of the form

$$\text{MSS} = C_1 \log(C_2 U_{10}^2) \qquad (7)$$

where C_1 and C_2 are coefficients. Phillips provides a range for C_1 spanning from 0.0046 to 0.015 depending on the surface roughness of the water [32, Sec. 4.7]. MSS is insensitive to the value of C_2, and depends heavily on the size of the waves and the speed of the wind.

Spectral bandwidth is a measure of the concentration of energy in a wave field at a single frequency. The more concentrated

or "peaky" the spectrum is, the narrower the bandwidth. Narrow band wave fields develop in strong constant winds, and tend to show group behavior in wave time series. The central wave within a group of sufficient steepness will break, transferring some portion of its energy to other wave frequencies and dissipating another portion as turbulence [33]. Multiple formulations of spectral bandwidth exist; the value used here is defined as follows:

$$\mathcal{V} = \sqrt{(m_0 m_2 / m_1^2) - 1}. \qquad (8)$$

The wave breaking results that follow will be related to the above bulk parameters in Section IV.

III. METHODS

SWIFT drifters were deployed by helicopter during five storms at PacWave, and allowed to drift freely. The SWIFTs integrate a Lord Microstrain 3DM-GX3-35 IMU. Using a complimentary filter, the IMU estimates sensor orientation in the global NWU reference frame from the measurements of three accelerometers, three magnetometers, and three gyroscopes oriented on sensor fixed orthogonal axes. The IMU also includes a synchronous global positioning system (GPS) receiver. Every 12 min, a burst of just under 9 min of acceleration and orientation data is sampled at 25 Hz. The 3 min in between sampling bursts are used by the SWIFTs to process and store the motion data. A small serial camera is located on a mast 0.3 m above the mean water line, when measured in still water, and looks down at a 45° angle. The camera takes a 240×320 pixel image of the water surface every 4–6 s during each data burst. While deployed, the SWIFTs can be tracked with an hourly Iridium satellite message that provides a GPS location, wave spectrum, and several bulk wave parameters including H_s and T_p. For all five storms, the SWIFTs were recovered washing ashore. Upon recovery, the raw acceleration and orientation data, recorded at 25 Hz, are available for download along with GPS position and velocity measurements sampled at 10 Hz. The drift tracks of the buoys are shown in Fig. 3. Two SWIFTs were deployed during each storm except for the February 2017 storm during which only one SWIFT was deployed. The SWIFT pairs remained in close proximity throughout the deployments (<0.5 km).

In postprocessing, the raw sensor accelerations are rotated into the NWU reference frame using the quaternion orientation data. The NWU acceleration data is then integrated and highpass filtered to determine the vector components of buoy velocity (**v**) and displacement (**r**). A fifth-order bidirectional Chebyshev type II filter was applied to the data after each integration step to remove sensor drift. The filter cutoff frequency was set to pass waves with period shorter than 30 s. The scalar wave spectrum and directional moments are calculated from the motion data using Welch's method [34]. For the four deployments where two SWIFTs were deployed, the SWIFTs remained in close proximity synchronously sampling data. The results from data bursts colocated in time were averaged to reduce spectral sampling noise. Bulk wave field parameters, such as H_s and T_p, were then calculated from the average spectrum for each 9 min data burst.

This article has been accepted for inclusion in a future issue of this journal. Content is final as presented, with the exception of pagination.

BROWN *et al.*: KINEMATICS AND STATISTICS OF BREAKING WAVES OBSERVED USING SWIFT BUOYS
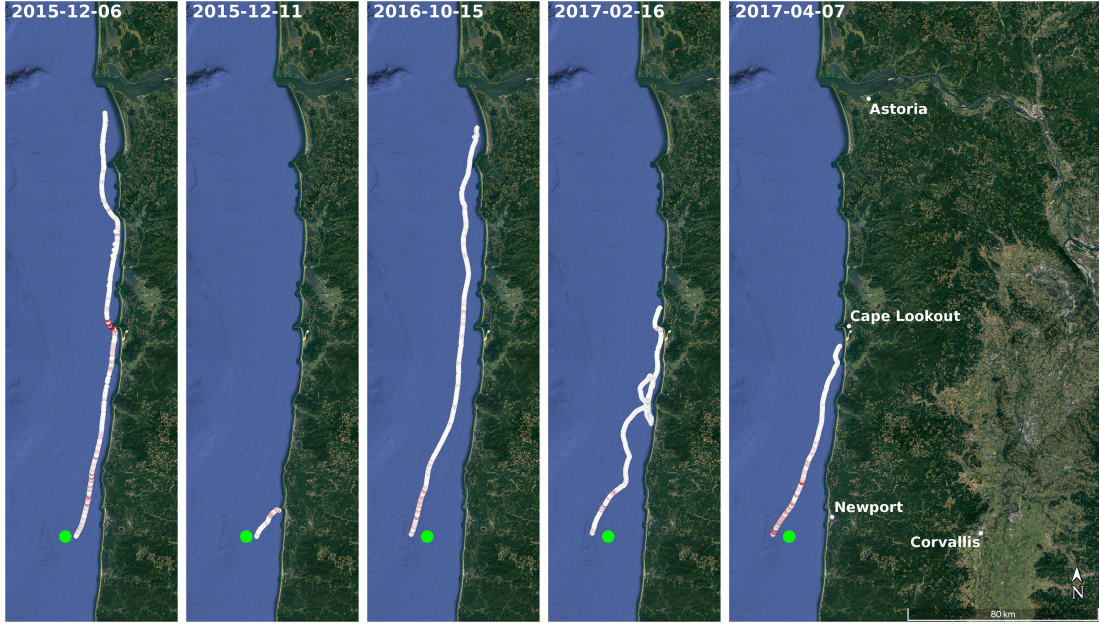
5

Fig. 3. SWIFT Tracks for the five deployments. The red color shading indicates the breaking fraction Q_b. The large green dot is the approximate location of PacWave.

A. Breaker Identification

The sensor within a wave measurement buoy measures the buoy's response to waves, it does not measure the waves themselves. For long period waves, the buoy very nearly follows the surface of the waves. As the period of the waves approach the natural frequency of the buoy (for SWIFTs $f_n \approx 1$ Hz), resonance occurs, and the measured displacement of the buoy will be greater than the vertical displacement of the water surface. Resonant behavior rapidly drops off above the natural frequency of the buoy, and the motion of the buoy will be less than the motion of the waves for frequencies greater than about twice the natural frequency of the buoy.

In linear seas, waves propagating at frequencies greater than 2 Hz are small capillary-gravity waves. This fact combined with the diminishing response of the buoy to high-frequency excitation results in noise dominating the accelerations measured at frequencies greater than 2 Hz. However, when a breaking wave impacts a buoy, components of acceleration greater than the buoy's natural frequency are excited. Capitalizing on this effect, Brown *et al.* developed three algorithms to identify breaking wave impacts in buoy acceleration data [35]. For the current work, only the short-time Fourier transform (STFT) method was used for breaker identification.

STFTs are often used in signal processing for the production of spectrograms [36]. As applied here, small windows of acceleration data (32 samples ≈ 1.5 s) are sequentially extracted from the greater time series. A Blackman Taper is applied to each component of acceleration within the window. The tapered acceleration window ($\mathbf{a}_{\mathrm{win}}$) is comprised of the north (a_N), west (a_W), and up (a_U) components of acceleration. The fast Fourier transform (FFT) is used to calculate the single sided amplitude spectrum for each component of $\mathbf{a}_{\mathrm{win}}$

$$\mathbf{a}(f) = \mathrm{FFT}(\mathbf{a}_{\mathrm{win}}). \qquad (9)$$

The amplitude of the complex values of $\mathbf{a}(f)$ are taken, and bins with frequency greater than or equal to 2 Hz are summed for each directional component, and then the component results are summed. The 2-Hz threshold was chosen to limit the influence of the buoy's resonant response on the detection algorithm

$$\alpha = \sum_{f > 2} |a_N(f)| + \sum_{f > 2} |a_W(f)| + \sum_{f > 2} |a_U(f)|. \qquad (10)$$

The resulting single value (α) with units of meter per second square is applied to the central point of the rolling window and used as a metric for breaking. The algorithm moves on to a window centered on the next data sample. Values of α are calculated for each point in the data burst, and a threshold is applied to α above which a breaking wave is indicated. Due to the window used, breaking cannot be indicated for the first or last 16 points of acceleration time series.

The 3.25-m/s^2 breaking threshold for α was initially set by iteratively examining the images that surround indicated breakers for visual corroboration of breaking. Large breakers entrain a significant amount of air in the water column, leaving large persistent bubble plumes and foam. Smaller breakers do not generate significant air entrainment, and are verified either by an image of the breaking crest or by the sudden appearance of surface foam. Due to the 4–6-s period between images, it was not possible to verify all indicated breakers near the breaking threshold. However, approximately 90% of the STFT-indicated breakers that occurred during daylight hours do show evidence of breaking in the surrounding images.

Fig. 4 shows both the measured motion and calculated α for a large breaking wave impact on a SWIFT. The impact of a large breaker typically imparts an intense initial acceleration on the SWIFT. This acceleration is usually due to the impact of a crest that is already breaking when it reaches the buoy.
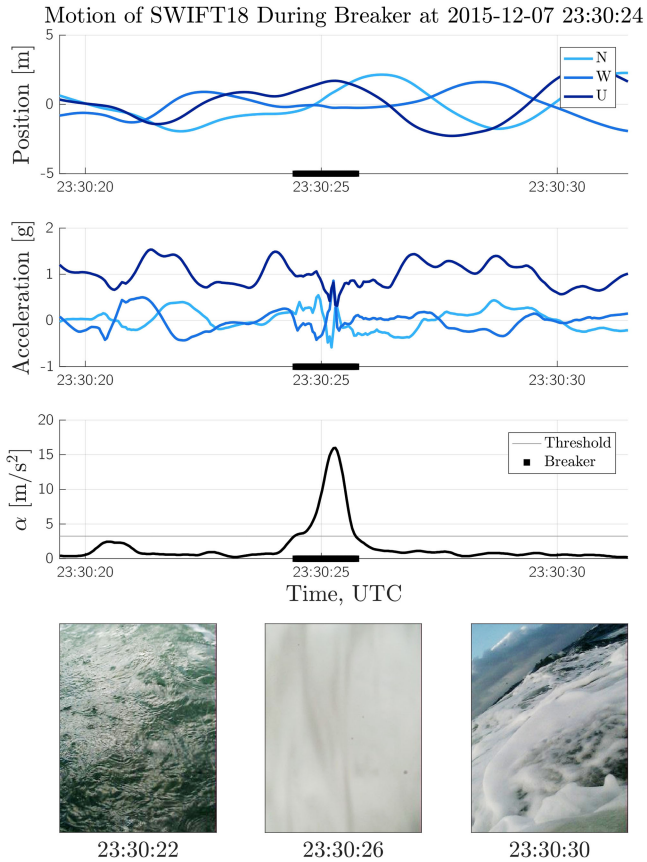
Fig. 4. Typical large breaking wave signal in panels of displacement (top), acceleration (middle), and α value (bottom). Pictures from the buoy mast are used to corroborate the signal.

Fig. 5. Typical small breaking wave signal in panels of displacement (top), acceleration (middle), and α value (bottom). Pictures from the buoy mast are used to corroborate the signal.

However, in rare cases the SWIFT can be swept in to the barrel of wave as it begins to break, and thrown forward resulting in a near zero g acceleration as the buoy falls forward of the crest. A high-amplitude decceleration is then observed as the buoy impacts the flat water in front of the wave. In both cases, the buoy will be over-topped by the crest, and rise to the surface in the turbulent bubble plume of the wave, which appears as low amplitude, high-frequency oscillations in the recorded accelerometer data [23].

The signature of small breakers in the acceleration data can be subtle. A quick initial impact acceleration can sometimes be observed in the data. However, the most common trait of a small breaking wave impact appears to be a rapid change in the direction of horizontal acceleration. The change occurs at a faster rate than would be expected in nonbreaking waves (see Fig. 5). The exact signature of a breaking wave depends heavily on the point in the breaking process at which the buoy is impacted. What was a large breaker may appear small if the buoy is impacted as the spilling crest subsides, and small breakers may still generate significant accelerations if the buoy is impacted as the wave begins to overturn. The random sampling of irregular waves most certainly affects the details of the signals identified.

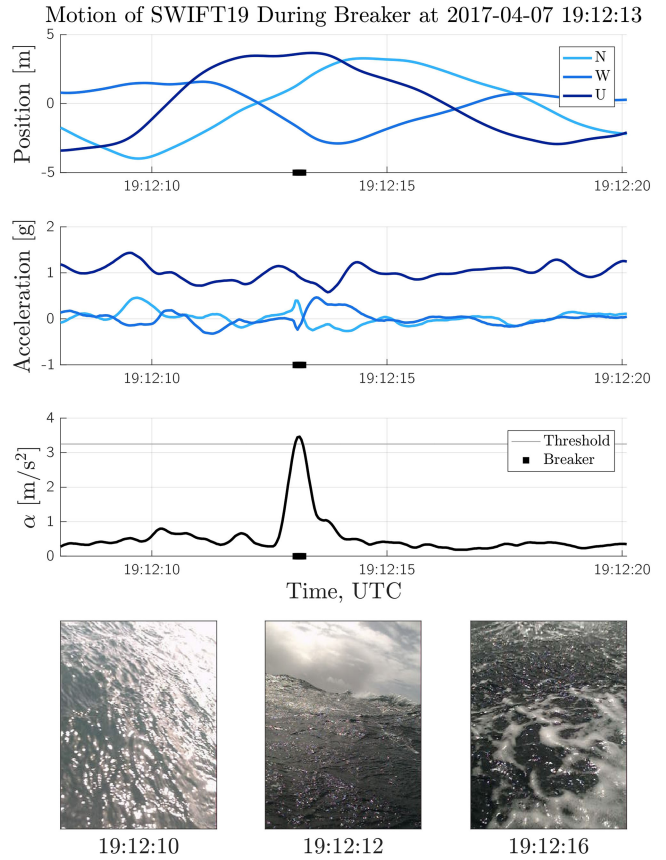The high-frequency signals used in the STFT method are distinct from the wave frequencies associated with the dissipation of wave energy during breaking (typically, $f_p < f < 5f_p$, see [37]). Rather, the high frequencies used in the STFT method are the response of the buoy to the impulsive forces of individual breaking waves. As such, the measured signal of a breaking wave will depend heavily on the size, shape, and natural frequency of the buoy. Therefore, the cutoff frequency, STFT window-size, and the α threshold will need to be adjusted, empirically, for application to other buoys.

The applicability of the breaker identification method to scientific and commercial wave measurement buoys will also depend on the internal sampling rates of those buoys. To capture the high-frequency accelerations imparted by breaking waves, an internal sampling rate substantially greater than the buoy's natural frequency will be required. Currently the default sampling rates of Datawell Waveriders (1.28 Hz) and Triaxys wave sensors (4 Hz) may not be sufficient to reliably identify breaking wave impacts. It is also true that the acceleration of a large 1 m diameter buoy impacted by a small whitecap may not be measurable. Smaller wave measurement buoys will be more capable of detecting wave breaking at small scales. The heuristic interpretation of the breaker detection method is a quantification of the instantaneous acceleration of a volume of surface water similar to the size of the buoy itself (i.e., a quasi-Lagrangian measure of the motion during breaking).

This article has been accepted for inclusion in a future issue of this journal. Content is final as presented, with the exception of pagination.

BROWN *et al.*: KINEMATICS AND STATISTICS OF BREAKING WAVES OBSERVED USING SWIFT BUOYS

7

B. Breaker Parameters and Statistics

In each 9-min burst of data, the breakers are identified and counted. Multiple parameters are calculated and recorded for each individual breaker. As the force acting on the SWIFT is approximately proportional to the acceleration of the SWIFT, the maximum linear acceleration ($\|\mathbf{a}\|_{\max}$) of the SWIFT is recorded as a proxy for the maximum impact force of the breaker on the SWIFT. The maximum value of α is also recorded, and may also be used as a metric for intensity as large waves generate more high-amplitude accelerations at high frequencies. The vertical elevation of the SWIFT relative to the still water level (SWL) at the beginning of each breaker is recorded as $\mathcal{Z}_0$, and the duration of the breaker is measured as the total time that α remains above the threshold for small breakers.

A value related to the work done on the SWIFTs by each breaker is also calculated. As work is equal to the force on an object times the distance moved, $\mathcal{W}$ is calculated as follows:

$$\mathcal{W} = \sum_{i=0}^{N} \|\mathbf{a}(t_i)\|^2 dt^2 \tag{11}$$

where $\|\mathbf{a}(t_i)\| dt^2$ is the change in the position of the SWIFT for each time step (dt). The incremental work of each time step between the up-crossing of the α threshold at t_0 and the down-crossing at t_N are summed. If the SWIFT motion is viewed as a Lagrangian measure of the surface water, then $\mathcal{W}$ may be closely related to the energy dissipated by a breaking wave. This latter connection will be pursued in a separate manuscript.

C. WAVEWATCH III (WW3) Modeling

WW3 wave forecasts were used to decide when to deploy the SWIFTs (i.e., which storms would have the best conditions). WW3 is a modeling system used to predict the generation, dissipation, and propagation of surface gravity waves. It is maintained and developed by the National Oceanic and Atmospheric Administrations, Silver Spring, MD, USA, National Center for Environmental Prediction (NCEP), Washington, DC, USA, as well as by academic and private users. WW3 is a third-generation wave-model that utilizes a spectral wave action balance equation and accounts for the modification of the wave field by the underlying bathymetry and ambient currents across the model grid and considers sink and source terms as well as the exchange of energy between spectral components. Recent advances (codified in WW3s ST4 physics package) have involved improvements to the parameterizations of dissipation associated with swell waves, wind waves, as well as shorter wave components that are affected by longer breaking waves [9]. More recent work (codified in the ST6 package) involves development of a new nonlinear wind input term that considers the dependence of the wave growth on wave steepness, airflow separation, and for negative growth rate under adverse winds [38]. The differences between the packages are fully described in the WW3 manual [39].

WW3 was used to model the five storms during which the SWIFTs were deployed. The primary input to WW3 is the wind-field, and the fidelity of the wave predictions are directly linked to the quality of the wind product [40]. Two different wind prod-

ucts were used, both of which are provided by NCEP. The two storms in December of 2015 were modeled using wind-fields from the climate forecast system (CFS), while the final three deployments in 2016 and 2017 were modeled with wind-fields from the global forecast system (GFS). GFS winds have a three hour time-resolution and $0.5° \times 0.5°$ spatial resolution. CFS winds have an increased spatial resolution of $0.204° \times 0.204°$, but the temporal resolution is poor with updates every 6 h. The same governing physics are used in both GFS and CFS; differences are therefore due to the differences in spatial and temporal resolution of the CFS wind product. The ST4 and ST6 physics packages were used to model the storms in this study. The ST4 package was used to model the 2015 storms, and the 2016 and 2017 storms were modeled with the newer ST6 physics package.

Although WW3 does not provide predictions collocated with the exact locations of the SWIFTs, wave spectra are extracted from the WW3 output by interpolating results from the model grid to the space and time locations that correspond to the SWIFT locations. This method is often applied for WW3 comparisons with stationary buoy data, and has also been successfully applied to comparisons with drifting buoys [40].

The SWIFT observations of bulk wave parameters are compared to those from the WW3 predictions for each storm, with a goal of using conventional bulk wave parameters to estimate the probability of wave breaking via empirical formula. Although wave-resolving models are more capable of capturing the underlying nonlinearity of the wave field and may therefore provide a better direct estimate of wave breaking, the goal is to evaluate the application of our results to existing operational products. Thus, application of our empirical relations to spectral wave model output is a potentially fast and efficient wave to provide statistical metrics on wave breaking to many ocean users.

IV. RESULTS

The breaking waves identified in the SWIFT data from the five storms at PacWave were counted and quantified in terms of intensity and probability. Section IV-A describes the relation of breaker severity to the bulk parameters of the wave field, whereas Section IV-B discusses the relation of Q_b to $\bar{S}$. Finally, in Section IV-C, the empirical relations determined from the five storms are applied to the model output to demonstrate breaking statistics as a potential operational product.

The five deployments are summarized in Table I. The storms were primarily intense offshore low pressure systems moving from south to north along the coast. The winds are amplified by the Oregon Coast Mountain Range, and form a strong south wind along the coast, which the National Weather Service refers to as the *coastal jet*. In turn, the coastal jet generates an alongshore current that drives the SWIFTs north. However, during the December 2015 storm, a strong low pressure system came to shore north of PacWave setting up strong onshore winds. Although strong, the winds were not amplified by the Coast Range, and drove the SWIFTs quickly to shore north of Newport, OR, USA (see Fig. 3).

The strongest storm began on April 7, 2017. The storm reached a maximum H_s of 8.0 m with $T_p = 12$ s and $T_m = 10$ s. The weakest storm was in February 2017, during which rela-

This article has been accepted for inclusion in a future issue of this journal. Content is final as presented, with the exception of pagination.
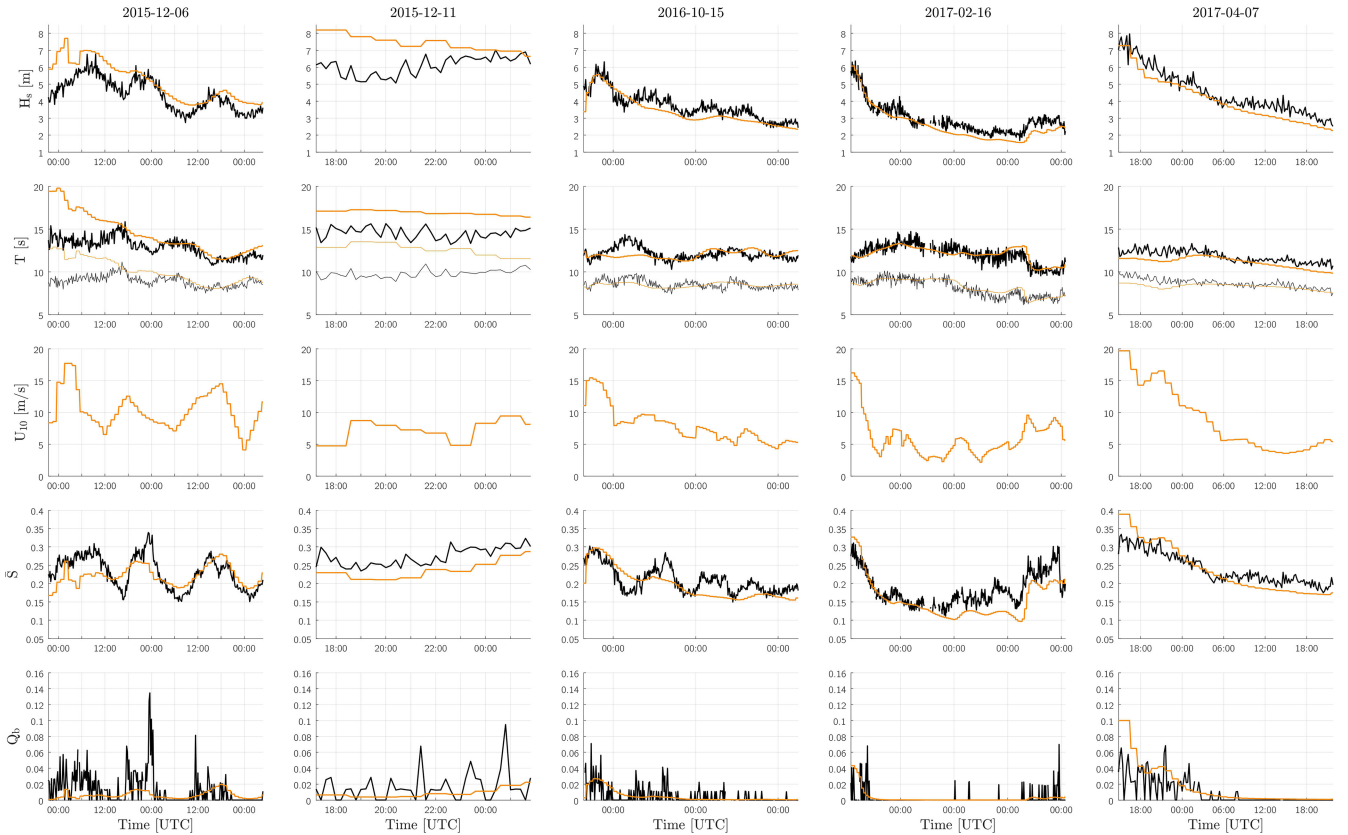
8

IEEE JOURNAL OF OCEANIC ENGINEERING

Fig. 6. Wave parameters during the five storms observed at PacWave (columns). The blue lines show the average results from the SWIFT buoys and the red/orange lines show the results from the WW3 model. T_p is shown as a dark line and T_m is given as a light line.

TABLE I
DEPLOYMENT INFORMATION AND NUMBER OF RECORDED BREAKERS

Year	2015		2016	2017		
Month-Day	12/06	12/11	10/15	02/16	04/07	Total
N SWIFTs	2	2	2	1	2	-
SWIFT-hrs	84	13	93	68	47	305
Max Hs	6.8	7.0	6.3	6.4	8.0	8.0
N Breakers	301	54	153	53	138	699

tively little breaking was identified. The storm rapidly weakened as the offshore low split into two systems with one moving further out to sea.

More than 772 breakers were identified in 305 h of recorded data. Bulk parameters for each storm are shown in Fig. 6. The majority of the breaking occurred near the beginning of each deployment while the storms were most energetic. Notable exceptions are during the December 2015 and February 2017 deployments, when the SWIFTs drifted past Cape Lookout (see Fig. 3). The Cape turns the alongshore current offshore, and the waves steepen due to the interaction with the amplified current. In strong currents, a moored buoy is effectively moving relative to the water, and can only measure the true steepness of the waves if the speed of the currents relative to the buoy are also known. However, as the SWIFTs drift with the current, they accurately measure the effective wave steepness.

A. Individual Breakers

In Fig. 7, the maximum linear acceleration of the SWIFT during each breaker is used as the independent variable to correlate with the other breaker specific parameters described in Section III-B. The maximum value of α during each breaker, the duration of the breaker, and $\mathcal{W}$ are all linearly related to $\|\mathbf{a}\|_{\max}$. $\mathcal{Z}_0$ increases only slightly with $\|\mathbf{a}\|_{\max}$, and is positively biased because crests break, not troughs. Although these parameters are autocorrelated through acceleration, they measure different kinematic aspects of the breaking wave.

In Fig. 8, the value of $\mathcal{W}$ for each breaker impact is plotted against several bulk parameters describing the background wave field. Much of the energy transported by a wave field moves as low-frequency swell, which is less steep and unlikely to release that energy in open ocean (deep water) breaking. T_p tends to follow the swell period. Most breaking occurs in wind waves with frequencies significantly greater than the peak wave frequency. T_m more closely follows the period of the waves that are likely to break. As such, the peak period T_p, is only weakly correlated with $\mathcal{W}$, and for brevity is not shown in Fig. 8. The probability of high $\mathcal{W}$ breakers is also positively correlated with $\bar{S}$. Conversely, increasing bandwidth $\mathcal{V}$ tends to decrease the probability of high $\mathcal{W}$ breakers, which suggests that group
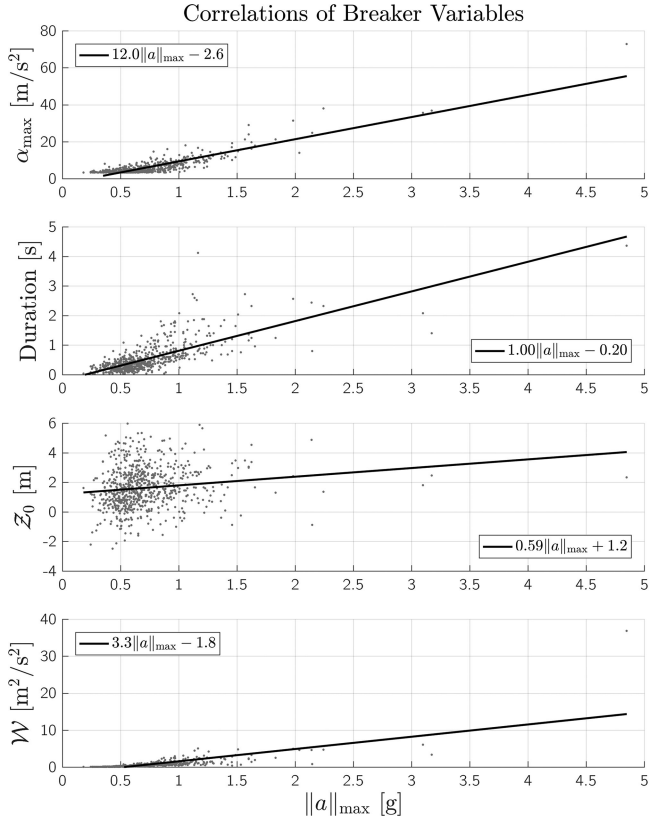
This article has been accepted for inclusion in a future issue of this journal. Content is final as presented, with the exception of pagination.

BROWN *et al.*: KINEMATICS AND STATISTICS OF BREAKING WAVES OBSERVED USING SWIFT BUOYS
9

Fig. 7. Maximum value of α, $\mathcal{Z}_0$, and $\mathcal{W}$ during individual breakers versus maximum acceleration during a breaker $\|\mathbf{a}\|_{\max}$.

behavior can lead to intense breakers. It has been suggested by Schwendeman and Thomson that the mean directional spread of the wave field also influences the probability of breaking [26]. However, in this study, mean directional spread did not show a strong correlation to either Q_b or the probability of high $\mathcal{W}$ breakers.

In Fig. 8, the linear fit to the raw data also fits the bin means of the raw data. This suggests that the mean $\mathcal{W}$ of breaking waves will increase linearly with H_s, T_m, and $\bar{S}$, and decrease linearly with increasing $\mathcal{V}$. Much of the variance around the mean trends in Fig. 8 is because the measured $\mathcal{W}$ of each breaking wave impact is highly dependent on the point in the evolution of a breaker at which the SWIFT was impacted. If the SWIFT is impacted at the moment of peak steepness just as a wave is beginning to break, the $\mathcal{W}$ of the breaker will be much larger than if an already spilling breaker impacts the float near the end of its evolution.

One exceptionally large breaker was recorded on December 11, 2015 at 22:29:33 UTC. The $\|\mathbf{a}\|_{\max}$ of the wave reached 4.8 g, and resulted in a $\mathcal{W}$ more than four times the next nearest wave. The breaker occurred in $H_s = 6.4$ m waves with $T_m = 10.3$ s. However, both $\bar{S}$ and $\mathcal{V}$ were very near their mean values for bursts where breaking occurred. This outlying wave demonstrates that high energy breakers can occur whenever large waves are breaking.

For each burst, the NWU accelerations of the SWIFTs were rotated about the vertical axis into a reference frame where

the major axis is aligned to the spectral peak wave direction. Histograms of acceleration were then determined for the major, minor, and vertical components of acceleration. An example of the resulting histograms is provided in Fig. 9. In linear sinusoidal seas, the motion of a water particle is Gaussian relative to a fixed point located on the SWL. As differentiation is a linear operation, component accelerations are also Gaussian. Breaking waves often impart accelerations that depart significantly from Gaussian probabilities, resulting in histograms with heavy tails. To determine if measured accelerations are outliers, an envelope calculated from the inverse binomial distribution is provided in Fig. 9. The envelope is drawn such that 99% of histograms generated from a random sampling of waves in that wave field would produce bin counts less than the indicated value.

Signal kurtosis (κ) is related to the fourth moment of a distribution, and is a measure of the weight of the tails of the distribution. A true Gaussian signal has a kurtosis of three. As waves become steep and break, the kurtosis of the acceleration signals will increase. If breakers are included in the calculation of kurtosis, intense breakers can have a very strong effect on kurtosis; the maximum value in this study is 127, although the vast majority of measurements are below five. When identified breakers are removed from the acceleration signal, the kurtosis provides a measurement of nonlinearity in the wave field (as does wave steepness). Q_b increases with the kurtosis of the non-breaking waves according to a power-law relation of the form $Q_b = 2.90(10)^{-7}\kappa_{\mathrm{mjr}}^{8.83}$.

B. Breaker Probability and Steepness

As a wave field increases in steepness, local energy concentrations are more likely to result in wave breaking. Fig. 10 shows the average SWIFT data for each burst relating Q_b to $\bar{S}$. Both MSS and $\bar{S}$ were defined and discussed in Section II-B. For the SWIFT measurements, the two measures of steepness are related linearly. The trends and dependences discussed apply to both measures of wave steepness, and for brevity, the results will focus primarily on $\bar{S}$.

Mean values of Q_b are shown for bins of $\bar{S}$. The values are shown at the center of their respective bins. The individual bursts show significant scatter around the mean Q_b of each bin, and the scatter is well fit by a Weibull Distribution. It is likely that sampling bursts for a longer period of time would reduce the burst-to-burst variance of Q_b measurements at the expense of reducing the stationarity of each data burst.

The relation of Q_b to $\bar{S}$ has empirically been shown by multiple authors to follow a power-law expression. A two-parameter power-law relation was proposed by Banner *et al.* [41]. Although the data presented by Zippel and Thomson were fit to the two-parameter expression by Banner *et al.*, they found that the second parameter was very nearly zero, reducing to a simple single-parameter expression [6]. The Zippel and Thomson's fit is shown in Fig. 10 for comparison.

For the SWIFT data in this study, we find the two-parameter power-law relation $Q_b = 7.42(\bar{S} - 0.095)^{3.52}$ best fits the observed breaker fractions. However, a single-parameter power-law relation $Q_b = 20.6\bar{S}^{5.48}$ demonstrates similar skill. These
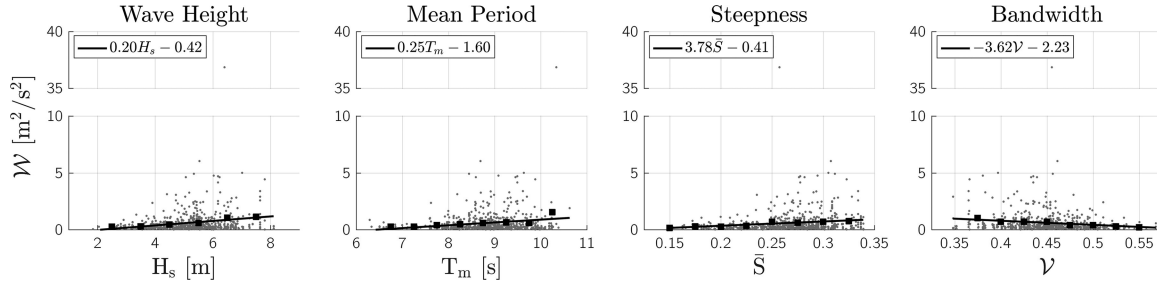
Fig. 8.   Linear work done on the SWIFT by the breaking wave ($\mathcal{W}$) versus the bulk parameters of the wave-field in which the breaker occurred (as measured by the SWIFTs). Black squares are bin averages and gray points are individual results. Lines show linear fits. The R^2 values of the linear fits to the bin means are: for H_s $R^2 = 0.864$, for T_m $R^2 = 0.621$, for $\bar{S}$ $R^2 = 0.888$, and for $\mathcal{V}$ $R^2 = 0.868$.
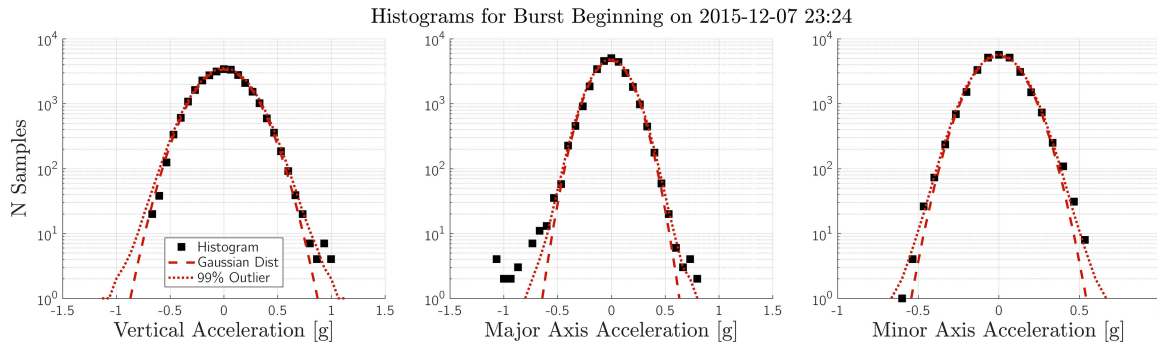

Fig. 9.   Histograms of acceleration during bursts with breakers (dots) and Gaussian fits to the distributions (lines). The observed histograms have longer tails than would be predicted by linear theory. The outlier envelopes for each fits (dashed lines) shows the value for each bin that 99% of bursts recorded at the same time, in the same random seas, would be less than.
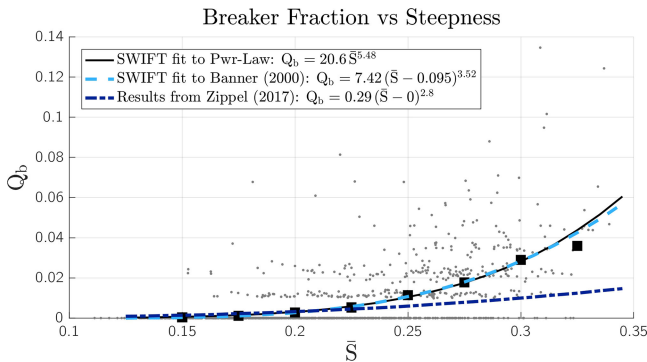

Fig. 10.   Breaker fraction versus bulk wave steepness. Small gray dot are the results from each of the 9-min data bursts. The large black squares are mean results binned by steepness $\bar{S}$. The lines are power-law fits to the binned results.

relations are significant, because they can allow breaker fraction to be estimated from conventional buoys or wave forecasts that provide $\bar{S}$ as a bulk parameter.

These relations are roughly similar to prior studies. However, in this study, significantly more breaking was observed for $\bar{S} > 0.2$, than was observed by Zippel and Thomson. It is possible that the results from Zippel and Thomson show less breaking due to under-sampling in the image-based breaker detection method of that study. Alternately, the Zippel and Thomson results may be very specific to wave breaking in intermediate water depth in the presence of sheared currents at a river mouth.

C. Comparison With WW3

The WW3 model output for the five storms during which the SWIFTs were deployed is shown in Fig. 6. The bulk steepness values $\bar{S}$, which are central to inferring wave breaking fraction from the parameters, have a general negative bias. However, the results vary according to the model generation and wind products used to force the wave forecast.

For the 2015 storms, using CFS winds with the ST4 physics package, WW3 overestimates H_s, T_p, and T_m at the beginning of the storms when the most energetic wave conditions are observed. The model results and observations become closer as the waves weaken, but the final error metrics over both storms indicate an appreciable overprediction, or positive bias, in bulk parameters (see Table II). Observations for the first 2015 storm include bulk steepness values ranging from 0.15 to 0.35 with oscillations between these two values over time scales of approximately a half day. Although the trends of wave steepness predicted by WW3 are well matched for this deployment, the model results predict variability in $\bar{S}$ that is not as pronounced, and the predicted oscillations appear damped and slightly phase-shifted when compared to observations. The $\bar{S}$ trends for the second 2015 storm are reproduced more accurately, but the overall values of $\bar{S}$ are underpredicted.

For the 2016 and 2017 storms, when lower resolution GFS winds are used in concert with the ST6 physics, WW3 results reproduce the observations of H_s, T_p, and T_m more accurately, although some variability over time scales of a day is not reproduced. Error metrics reported in Table II confirm this

TABLE II
PERCENT ERROR FOR THE WW3 PREDICTIONS OF THE BULK
WAVE PARAMETERS

|	2015 (CFS & ST4)		2016-2017 (GFS & ST6)	
	% Error	% Bias	% Error	% Bias
H_s	23.5	18.4	15.6	-11.1
T_p	17.6	12.5	10.5	2.5
T_m	21.3	15.4	6.6	-0.1
$\bar{S}$	15.8	-3.3	18.5	-9.7
MSS	28.4	-8.2	36.4	-23.6

Fig. 11. MSS measured by the SWIFTS and estimated from the WW3 spectral output. The data were fit to the log relation provided by Phillips [32, Sec. 4.7].
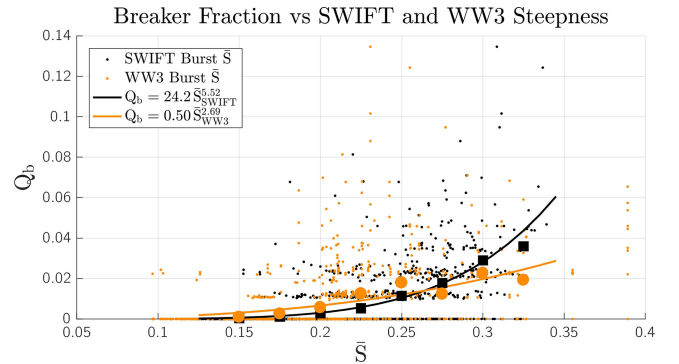

Fig. 12. Breaking fraction versus steepness, with an empirical fit applied to WW3 model steepness values. Inaccuracy in the WW3 $\bar{S}$ values leads to increased scatter in the determination of Q_b.

interpretation. This implies that, for predicting wave height and period, any benefits derived from using higher resolution CFS winds may be outweighed by the improved accounting of wave growth and dissipation provided by the ST6 physics package. However, despite the improvement in predicting H_s and period, the predictions of $\bar{S}$ and MSS (quantified in Table II) do not improve for the 2016 and 2017 deployments. In particular, observed variability in wave steepness over time scales of approximately a day appear more drastic in the observations compared to the values predicted by WW3. However, we note that the general trends in $\bar{S}$ for the 2017 storms are reproduced by the model results.

In the bottom panels of Fig. 6, the empirical two-parameter power-law fit of Q_b to $\bar{S}$ for the SWIFT data ($Q_b = 7.42(\bar{S} - 0.095)^{5.48}$) was used to generate a prediction of Q_b given the WW3 estimate of $\bar{S}$.

Although the resulting predictions of Q_b tend to follow the trends of the observed Q_b, the accuracy of the predictions is poor. As Q_b depends roughly on the cube of $\bar{S}$, inaccuracies in the WW3 prediction of $\bar{S}$ lead to significant error in the estimate of Q_b. This can clearly be seen as the SWIFTs pass Cape Lookout during the December 2015 storm. At that time, the SWIFTs recorded their highest observed Q_b. This may potentially be related to a strong offshore current that can form near the Western prominence of the Cape that causes the waves traveling to the East to steepen and break. Predicting such circulations and coupling WW3 with these circulation predictions could potentially improve wave steepness predictions.

In Fig. 11, the MSS observed by the SWIFTs is compared to the MSS predicted using WW3 results at the location of the SWIFTs. The values of MSS from the SWIFTs and from WW3 are related to the wind speed, which was also obtained from WW3 at the location of the SWIFTs. The SWIFT data are well fit by the log relation provided by Phillips [32, Sec. 4.7]. The MSS observed by the SWIFTs appears to flatten out near a value between 0.015 and 0.02. Although greater steepness values could theoretically be observed, the necessary wind speed quickly becomes extreme. WW3 tends to underestimate MSS at low wind speeds and overestimate MSS at wind speeds above 13 m/s. For that reason, a linear fit to the WW3 MSS (not
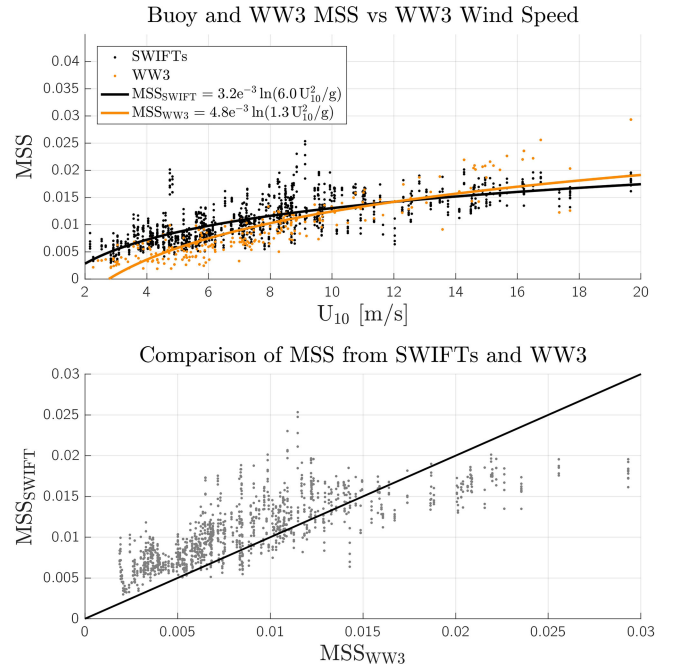
shown) shows marginally more skill than the shown log relation. In the top panel, there are more data points from the SWIFT measurements than from WW3 because WW3 only updates the wind speed and the wave spectrum at most every hour, while the SWIFTs provide an estimate five times per hour, leading to increased measurement scatter.

The Q_b observed by the SWIFTs is shown in Fig. 12 compared to the value of $\bar{S}$ measured by the SWIFTs (black dots), and predicted using WW3 results (orange dots). As in Fig. 10, bin means are shown with large dots, and the power-law fit to the burst data is shown as a line. Although some over-estimates of $\bar{S}$ can be seen, the inaccuracies of WW3 lead primarily to an underestimation of $\bar{S}$, which also leads to an underestimate of Q_b. The power-law fit of the WW3 data tends to overestimate the amount of breaking at low $\bar{S}$, and underestimate the breaking at high $\bar{S}$.

This article has been accepted for inclusion in a future issue of this journal. Content is final as presented, with the exception of pagination.

12   IEEE JOURNAL OF OCEANIC ENGINEERING

V. Conclusion

This paper uses an algorithm to identify the transient, high-frequency acceleration signals of breaking wave impacts on SWIFT wave measurement buoys. When possible, images from cameras on-board the SWIFTs were used to verify that the detected acceleration signals were due to breaking waves. The method was applied to a dataset recorded off the coast of Oregon during five large winter storms.

Individual breaking waves were identified, and the probability of wave breaking was calculated and reported as breaking fraction (Q_b). Following previous studies, the breaking fraction exhibits a power law relation to the steepness of the background wave field [6], [41], and this relation can be applied to infer breaking fraction from conventional wave measurements or wave forecasts. However, this is shown to be very sensitive to accuracies in the bulk wave steepness, which in turn may be sensitive to the wind forcing used to obtain the wave forecast. With a more accurate bulk wave slope from the forecast, it should be possible to predict the basic statistics of breaking. This would be of operational use to mariners and engineers across a wider range of fields.

Several new breaking metrics were defined and evaluated, including the duration of the breaker, the maximum acceleration of the buoy during the breaker, and a proxy for the work done by the breaker ($\mathcal{W}$). There is strong variability in each of these metrics, in part because the buoy can be impacted at any phase of the evolution of a breaker. Still, $\mathcal{W}$ does increase with the bulk wave field parameters H_s, T_m, $\bar{S}$, and decrease with bandwidth $\mathcal{V}$. $\mathcal{W}$ may also be related to the energy dissipated by the wave, and the link between the average $\mathcal{W}$ and the wave-averaged spectral dissipation due to breaking will be investigated in future work.

The breaker detection method used for this analysis is suitable for real-time detection on-board commercial and government wave measurement buoys. With the advent of low-cost, fast-sampling IMUs, and the computational efficiency of Fourier transformations, this would not dramatically change the design or engineering of existing buoys. Breaker fraction and intensity could then become standard wave field statistics reported throughout multiyear deployments. Such an advancement in wave measurement technology would vastly increase the breaking wave data available to scientists and engineers.

Acknowledgment

References

[1] R. M. Carson, "On the capsize performance of a discus buoy in deep sea breakers," *Ocean Eng.*, vol. 9, no. 5, pp. 501–514, Jan. 1982.

[2] J. Hovland, R. K. Paasch, and M. C. Haller, "Characterizing dangerous waves for ocean wave energy converter survivability," in *Proc. ASME 29th Int. Conf. Ocean, Offshore Arctic Eng.*, Jun. 2010, p. 8.

[3] G. Cuomo, R. Piscopia, and W. Allsop, "Evaluation of wave impact loads on caisson breakwaters based on joint probability of impact maxima and rise times," *Coastal Eng.*, vol. 58, no. 1, pp. 9–27, Jan. 2011.

[4] M. A. Chella, A. Tørum, and D. Myrhaug, "An overview of wave impact forces on offshore wind turbine substructures," *Energy Procedia*, vol. 20, pp. 217–226, Jan. 2012.

[5] S. Marx *et al.*, "Probabilistic safety assessment of offshore wind turbines," ForWind for the Ministry for Science and Culture in Lower Saxony, pp. 1–161, Feb. 2015.

[6] S. Zippel and J. Thomson, " Surface wave breaking over sheared currents: Observations from the mouth of the Columbia River," *J. Geophys. Res., Oceans*, vol. 122, no. 4, pp. 3311–3328, Apr. 2017.

[7] W. K. Melville, "The role of surface-wave breaking in air-sea interaction," *Annu. Rev. Fluid Mech.*, vol. 28, no. 1, pp. 279–321, 1996.

[8] E. Lamarre and W. K. Melville, "Air entrainment and dissipation in breaking waves," *Nature*, vol. 351, no. 6326, pp. 469–472, 1991.

[9] F. Ardhuin *et al.*, "Semiempirical dissipation source functions for ocean waves. Part I: Definition, calibration, and validation," *J. Phys. Oceanogr.*, vol. 40, no. 9, pp. 1917–1941, Apr. 2010.

[10] P. A. E. M. Janssen, "Progress in ocean wave forecasting," *J. Comput. Phys.*, vol. 227, no. 7, pp. 3572–3594, Mar. 2008.

[11] A. C. Brown, "Wave energy: Considering the waves," *Shore Beach*, vol. 81, no. 4, pp. 12–22, Dec. 2013.

[12] J. Thomson, "Wave breaking dissipation observed with "SWIFT" drifters," *J. Atmos. Ocean. Technol.*, vol. 29, no. 12, pp. 1866–1882, Dec. 2012.

[13] M. Smith and J. Thomson, " Scaling observations of surface waves in the Beaufort Sea," *Elementa Sci. Anthropocene*, vol. 4, Apr. 2016.

[14] T. H. C. Herbers, P. F. Jessen, T. T. Janssen, D. B. Colbert, and J. H. MacMahan, "Observing ocean surface waves with GPS-tracked buoys," *J. Atmos. Ocean. Technol.*, vol. 29, no. 7, pp. 944–959, Mar. 2012.

[15] J. Thomson, M. S. Schwendeman, S. F. Zippel, S. Moghimi, J. Gemmrich, and W. E. Rogers, "Wave-breaking turbulence in the ocean surface layer," *J. Phys. Oceanogr.*, vol. 46, no. 6, pp. 1857–1870, Mar. 2016.

[16] M. S. Schwendeman and J. Thomson, "Sharp-crested breaking surface waves observed from a ship-based stereo video system," *J. Phys. Oceanogr.*, vol. 47, no. 4, pp. 775–792, Feb. 2017.

[17] M. S. Longuet-Higgins and N. D. Smith, "Measurement of breaking waves by a surface jump meter," *J. Geophys. Res.*, vol. 88, no. C14, pp. 9823–9831, 1983.

[18] J. R. Gemmrich and D. M. Farmer, "Observations of the scale and occurrence of breaking surface waves," *J. Phys. Oceanogr.*, vol. 29, no. 10, pp. 2595–2606, Oct. 1999.

[19] M. A. Weissman, S. S. Atakturk, and K. B. Katsaros, " Detection of breaking events in a wind-generated wave field," *J. Phys. Oceanogr.*, vol. 14, no. 10, pp. 1608–1619, 1984.

[20] R. W. Pascal *et al.*, "A spar buoy for high-frequency wave measurements and detection of wave breaking in the open ocean," *J. Atmos. Ocean. Technol.*, vol. 28, no. 4, pp. 590–605, Apr. 2011.

[21] R. Balaji, S. A. Sannasiraj, and V. Sundar, "Identification of breaking events from the responses of a data buoy," *Proc. Inst. Mech. Eng. M, J. Eng. Maritime Environ.*, vol. 224, no. 2, pp. 127–139, Jun. 2010.

[22] A. Sinclair, "FlowRider: A lagrangian float to measure 3-D dynamics of plunging breakers in the surf zone," *J. Coastal Res.*, vol. 293, pp. 205–209, Jan. 2014.

[23] A. Brown, "The effects of ocean variability and breaking waves on wave energy converter reliability and survivability," Ph.D. dissertation, Oregon State Univ., Corvallis, OR, USA, Jul. 2014.

[24] "Datawell Waverider Reference Manual: WR-SG, DWR-MkIII, DWR-G," Oct. 2009.

[25] C. MacIsaac and S. Naeth, "TRIAXYS next wave II directional wave sensor the evolution of wave measurements," in *Proc. Oceans Conf.*, Nov. 2013, pp. 1–8.

[26] M. Schwendeman and J. Thomson, " Observations of whitecap coverage and the relation to wind stress, wave slope, and turbulent dissipation," *J. Geophys. Res., Oceans*, vol. 120, no. 12, pp. 8346–8363, Dec. 2015.

[27] M. Schwendeman, J. Thomson, and J. R. Gemmrich, "Wave breaking dissipation in a young wind sea," *J. Phys. Oceanogr.*, vol. 44, no. 1, pp. 104–127, Jan. 2014.

[28] M. J. Tucker and E. G. Pitt, *Waves in Ocean Engineering*. Amsterdam, The Netherlands: Elsevier, 2001.

This article has been accepted for inclusion in a future issue of this journal. Content is final as presented, with the exception of pagination.

BROWN *et al.*: KINEMATICS AND STATISTICS OF BREAKING WAVES OBSERVED USING SWIFT BUOYS

13

[29] A. Toffoli, A. Babanin, M. Onorato, and T. Waseda, " Maximum steepness of oceanic waves: Field and laboratory experiments," *Geophys. Res. Lett.*, vol. 37, no. 5, pp. 1–4, Mar. 2010.

[30] A. Chawla and J. T. Kirby, "Monochromatic and random wave breaking at blocking points," *J. Geophys. Res., Oceans*, vol. 107, no. C7, 2002, pp. 4-1–4-19.

[31] M. L. Banner and R. P. Morison, "Refined source terms in wind wave models with explicit wave breaking prediction. Part I: Model framework and validation against field data," *Ocean Model.*, vol. 33, no. 1/2, pp. 177–189, 2010.

[32] O. M. Phillips, *The Dynamics of the Upper Ocean*. London, U.K.: Cambridge Univ. Press, 1966.

[33] W. K. Melville, "The instability and breaking of deep-water waves," *J. Fluid Mech.*, vol. 115, pp. 165–185, 1982.

[34] P. Welch, "The use of fast Fourier transform for the estimation of power spectra: A method based on time averaging over short, modified periodograms," *IEEE Trans. Audio Electroacoust.*, vol. 15, no. 2, pp. 70–73, Jun. 1967.

[35] A. C. Brown, J. Thomson, T. Özkan Haller, M. C. Haller, and A. Ellenson, "Breaking waves observed during storms at a wave energy test site," in *Proc. 12th Eur. Wave Tidal Energy Conf.*, Cork, Ireland, Aug. 2017, pp. 1–8.

[36] J. Allen, "Applications of the short time Fourier transform to speech processing and spectral analysis," in *Proc. IEEE Int. Conf. Acoust., Speech, Signal Process.*, May 1982, vol. 7, pp. 1012–1015.

[37] O. M. Phillips, "Spectral and statistical properties of the equilibrium range in wind-generated gravity waves," *J. Fluid Mech.*, vol. 156, pp. 505–531, 1985.

[38] S. Zieger, A. V. Babanin, W. Erick Rogers, and I. R. Young, "Observation-based source terms in the third-generation wave model WAVEWATCH," *Ocean Model.*, vol. 96, pp. 2–25, Dec. 2015.

[39] W. I. D. G. (WW3DG), "WaveWatch III. user manual v5.16," Oct. 2016.

[40] A. Ellenson and T. Özkan Haller, "Predicting large ocean wave events characterized by bi-modal energy spectra in the presence of a low-level southerly wind feature," *Weather Forecasting*, 2018.

[41] M. L. Banner, A. V. Babanin, and I. R. Young, "Breaking probability for dominant waves on the sea surface," *J. Phys. Oceanogr.*, vol. 30, no. 12, pp. 3145–3160, 2000.

Ashley Ellenson received the B.S. degree in environmental engineering from Columbia University, New York, NY, USA, in 2011, and the M.S. degree in coastal and ocean engineering from Oregon State University, Corvallis, OR, USA, in 2017. She is currently working toward the Ph.D. degree at the Department of Coastal and Ocean Engineering, School of Construction and Civil Engineering, Oregon State University.

Her research interests include wave prediction, the quantification of uncertainty in wave models, and data assimilation in sediment erosion forecasts.

Fadia Ticona Rollano received the B.S. degree in civil engineering from The University of Kansas, Lawrence, KS, USA, in 2014. She is working toward the M.S. degree in civil engineering at the School of Civil and Construction Engineering, Oregon State University, Corvallis, OR, USA.

She worked for two years as a Civil Engineer in Training with HDR Engineering, Inc., MO, USA. She is currently a Graduate Research Assistant with the School of Civil and Construction Engineering, Oregon State University. Her research focuses on the behavior of wave dissipation in extreme sea states using field data and numerical models.

H. Tuba Özkan-Haller received the B.S. degree in civil engineering from Boğaziçi University, Istanbul, Turkey, in 1991, and the M.C.E and Ph.D. degrees in civil engineering from the University of Delaware, Newark, DE, USA, in 1994 and 1998, respectively.

She was a Postdoctoral Scholar with the University of Cantabria, Cantabria, Spain, and spent three years as a faculty member with the Department of Naval Architecture and Marine Engineering, University of Michigan, before arriving at Oregon State University. She has helped develop several community models for the prediction of nearshore wave and circulation fields, and has also taken part in several field and laboratory studies aimed at validating these models. She is currently a Professor and an Associate Dean for Research and Faculty Advancement, the College of Earth, Ocean, and Atmospheric Sciences, Oregon State University, Corvallis, OR, USA, and also holds an appointment with the School of Civil and Construction Engineering. Her research interests include wave prediction, wave-structure interaction, wave-induced currents, and transport of tracers and sediment.

Adam Brown received the Ph.D. degree in mechanical engineering from Oregon State University, Corvallis, OR, USA, in 2014.

He completed his postdoctoral research with the Applied Physics Laboratory, University of Washington, Seattle, WA, USA, in 2018. His research focuses on understanding the operational environment and hydrodynamic behavior of offshore renewable energy systems.

Jim Thomson received the Ph.D. degree in applied ocean physics from the Massachusetts Institute of Technology/Woods Hole Oceanographic Institution joint program, Woods Hole, MA, USA, in 2006.

In 2006, he joined the Applied Physics Laboratory, University of Washington, Seattle, WA, USA. In 2009, he began a joint appointment with the Faculty of Civil and Environmental Engineering, where he currently teaches fluid mechanics and coastal engineering. His research interest focuses basic and applied ocean research, with an emphasis on field measurements of waves, currents, and turbulence.

Dr. Thomson is a member of the Northwest National Marine Renewable Energy Center, where he is applying his interest techniques to characterize sites for marine energy development.

Merrick C. Haller received the Ph.D. degree in civil engineering from the University of Delaware, Newark, DE, USA, in 1999.

Before joining Oregon State University (OSU) Corvallis, OR, USA, in 2001, he spent two years in the Remote Sensing Industry. He is currently the Interim Director of the Northwest National Marine Renewable Energy Center, OSU, Corvallis, OR, USA, and a Professor and an Associate Head with the School of Civil and Construction Engineering. His research focuses on the development of remote sensing techniques for the study of wave breaking, rip currents, and wave-current interactions in the littoral zone (Photo credit: Jim Carroll.).